Benchmark study of undrained triaxial testing of Opalinus Clay shale: Results and implications for robust testing

Alberto Minardi [a], Silvio B. Giger [b,*], Russell T. Ewy [c], Rudy Stankovic [d], Jørn Stenebråten [e], Magnus Soldal [f], Marco Rosone [g], Alessio Ferrari [a,g], Lyesse Laloui [a]

[a] *Swiss Federal Institute of Technology EPFL, Lausanne, Switzerland*
[b] *National Cooperative for the Disposal of Radioactive Waste, Wettingen, Switzerland*
[c] *Chevron Energy Technology Co., Richmond, CA, USA*
[d] *Rock Soil testing and Development Company, Park City, UT, USA*
[e] *SINTEF, Trondheim, Norway*
[f] *Norwegian Geotechnical Institute, Oslo, Norway*
[g] *Università degli Studi di Palermo, Palermo, Italy*

ABSTRACT

Triaxial testing of argillaceous rocks and shales is significantly more challenging than conventional rock mechanical testing. The challenges are mainly related to the very low permeability of these geomaterials, and their sensitivity to exposure of atmosphere and brines, which induces variations of water content, suction and effective stress. There are currently no international standards to guide service laboratories for robust testing procedures for shales. A benchmark study of undrained triaxial testing was therefore initiated with three leading service laboratories in shale testing, performing 13 tests and using two different methods of establishing sample saturation prior to deformation. Both methods paid particular attention to minimize volume expansion of the specimens during saturation, and the loading rate during the shear phase in all tests was selected based on intrinsic sample properties and drainage configurations to ensure pore fluid pressure equilibration across the specimen. Opalinus Clay shale core material from the Mont Terri underground research laboratory was used for testing specimens, and intervals on cores were pre-selected on the basis of computer tomography to minimize material heterogeneity. A detailed diagnostic analysis of all tests was performed, and a comparison of the testing results is presented. Good reproducibility of the effective stress paths was achieved by the different laboratories for tests at identical or near-identical initial effective stress conditions. In particular, the test results over a larger range of effective stresses indicate very similar evolution of the fluid pressure during testing and a consistent picture for the derivation of global material properties. On the example of Opalinus Clay, the study demonstrates that robust triaxial testing results can be achieved for shales if some key challenges are adequately addressed.

1. Introduction

Triaxial testing is a critical method to assess the mechanical behaviour and determine material properties for geomechanical applications. The key advantage of this testing method with respect to in situ testing is that the effective state conditions (effective stresses) can be monitored, provided that the pore pressure throughout the specimen of porous materials is in equilibrium. This is a challenge for claystones or shales due to their very small pore sizes (tens of nanometres), and ultimately the low permeabilities (nanodarcies or lower). A further complication is the complex chemo-mechanical properties of clay particles.

Volumetric changes of test specimens may therefore be related to changes of applied stresses but also from interactions of clay particles with the synthetic brines. In essence, soil mechanical approaches must be considered for triaxial testing of shales but extended to elevated pressures more typical of rock mechanics. The requirements for robust testing for such materials are therefore greater than for conventional rock mechanics testing.[1]

When considering triaxial testing of shale specimens, three key aspects need increased attention: (1) sampling and handling of core material, (2) ensure saturation of specimens in the rig prior to the deformation phase, and without affecting the specimen's properties by doing so, and (3) selecting an appropriate loading rate to ensure equilibrated pore pressure across the specimen.

* Corresponding author.
E-mail address: silvio.giger@nagra.ch (S.B. Giger).

Guidelines for preservation of shale cores, sampling and handling were recently published by Ref. 2. Several experimental studies have demonstrated the impact of water saturation on the mechanical response of shales. Both strength and stiffness can be significantly overestimated if saturated conditions are not established. Examples can be found in Refs. 3–10 for shales and claystone, and in Refs. 11–13 for gas shales. However, when saturation is established at low effective stress, this is often associated with significant volume increase and may lead to an alteration of the specimen's structure and eventually to irreversible changes of its material properties. Clear experimental evidence of this aspect have been reported in several studies related to specimens' exposure to uncontrolled relative humidity air[14–18] and synthetic fluid.[2,19] These studies have confirmed the need of a careful handling of shale cores and test specimens in the laboratory.[2,20] Finally, the determination of the appropriate loading rate is the critical aspect of shale triaxial testing during shear phase, for both drained and undrained conditions. Deviatoric loading of the specimens is usually performed with a constant axial strain rate, which should be selected such that pore pressure equilibration is warranted within the specimen. This depends on the sample's capacity to dissipate pore fluid pressure (essentially controlled by its permeability) and the dissipation distance (controlled by sample size and drainage configuration) (e.g. Refs. 20, 21). For the case of Opalinus Clay shale, the designated host rock for high-level radioactive waste in Switzerland, Ref. 22 have demonstrated that for undrained testing a strain rate one order of magnitude greater than the one theoretically appropriate for good pore pressure equilibration led to an apparent strength increase of 20% and a decrease in Poisson's ratio of 70%. The appropriate loading rate should therefore be calculated for each shale under investigation. It should also be the basis for a serious estimation of test duration by service laboratories prior to shale testing campaigns.

For the case of Opalinus Clay, triaxial testing procedures were recently improved to respect the above aspects: Ref. 23 focused on securing proper sample saturation prior to deformation, and Ref. 24 in addition ensured this step is not associated with significant volume increase. Finally, Ref. 22 used a different method, pioneered by Ref. 25 and refined by Ref. 26, without the need of adding an external pore fluid for undrained testing, hence avoiding some of the testing complexity. Despite these recent advances, the absence of formal international standards to guide research and service laboratories in shale testing, and the slight differences in the testing methods may still cast doubts on the robustness of some of the applied testing protocols.

In this study, a direct comparison of undrained triaxial testing was organized involving three leading service laboratories in shale testing. In a first step, two different testing protocols were adopted, drawing on the recent experience especially by Refs. 22, 24, and honouring all identified key aspects as emphasized above. The ultimate goal was to substantiate that robust and reproducible test results can be achieved by different labs and using different testing methods, thereby increasing confidence in the testing results.

2. Materials and methods

2.1. Testing programme

The benchmark study of consolidated and undrained (CU) triaxial testing involved three different laboratories, named in the following as Lab A, Lab B, and Lab C. Different stress paths were adopted in the study, but only the more widely used axial compression tests (increase of axial load while keeping total radial stress constant) are presented in this paper to focus on the testing methodology. To explore the anisotropic structure of

Table 1

Overview of the experimental programme with the list of the different tests performed by the three laboratories. 'S' and 'P' refer to sample orientations relative to bedding, and the numeric value refers to mean effective stress at the start of shearing (see text).

Testing Series	Lab A	Lab B	Lab C
Series 1	AS4	BS4 BP4	–
Series 2	AS10a AS10b AP12	BS10	CS7 CP9
Series 3	AS16	BS16	CS17 CP17

Opalinus Clay, the tests were carried out by axially loading the specimens with two different configurations: loading perpendicular (S-tests) and parallel (P-tests) to the bedding orientation. As the study targeted the comparison of the results obtained from tests performed in the same conditions, three different initial effective confining stresses (p'_{in}) were selected: 4, 10, and 16 MPa. Some deviation from these values occurred for some of the tests, and they are highlighted later in the text. For all the tests, a target pore fluid pressure equal to approximately 5 MPa was achieved to ensure full dissolution of potential air trapped in the system,[27] i.e. stability of the fluid compressibility.

An overview of the experimental programme is presented in Table 1; the three series of tests corresponding to the three different confining stresses are highlighted and a code is given to each test to better identify the data producer (letters A to C), the loading direction with respect to bedding orientation (S or P) and the value of effective mean stress (p'_{in}) in units of Megapascals at the start of the shear phase. For the S-tests, each lab performed two to four tests and a direct comparison of test results at the same or similar testing conditions (i.e. same consolidation stress, pore fluid pressure) was envisaged. In contrast, for the P-tests, only one test was performed per lab (with the exception of Lab C, conducting two tests), and the shear phase in each test was starting from a different effective mean stress. Hence the comparison of test results for P-tests is indirect and focuses on the consistency of the trends of test results.

2.2. Tested material and specimen preparation

Opalinus Clay from the so called «shaly facies»[28] at the Mont Terri underground laboratory was used for the experimental programme. Cores of approximately 30 to 40 cm length and 10 cm diameter were recovered from the borehole BGC2 at a coring depth between 29 and 34 m below the tunnel floor, approximately 270 m below ground. The cores were immediately resin-impregnated in a PVC barrel to keep them preserved (cf. Ref. 22). To provide each participating laboratory with very similar core material and to verify core integrity prior to shipping, all cores were analysed using medical X-ray computer-tomography (XCT). Details of the applied XCT method can be found in Ref. 29, and an example of a virtual cross-section of core BGC2-34 is presented in Fig. 1. It is noted that the CT-number is a proxy for material density. The virtual cross-section was the basis to select intervals for sub-coring.

Specimens' size for testing was either 19 mm diameter and 38 mm length (Lab C) or 25 × 50 mm (Labs A and B) and therefore smaller than typical plug size of triaxial testing in rock and soil mechanics. This was to reduce the drainage path length (during consolidation) and the pore pressure dissipation length (during shearing), respectively, enabling individual tests to be conducted in typically one to two weeks rather than several weeks to months (see Section 2.3).
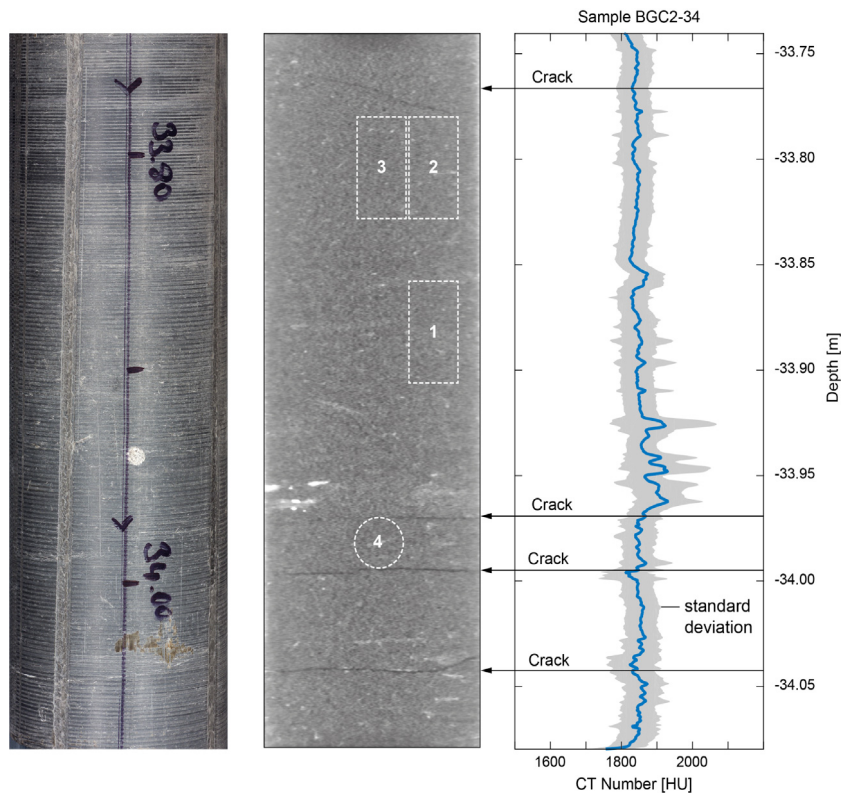
Fig. 1. CT-scan of the core BGC2-34 (left side) used by Lab B to select the zone for sub-coring the specimens.

The extraction of the specimens from the cores was done by drilling. Different types of cooling lubricant fluids were used by the laboratories for sub-coring the specimens: Marcol 52 oil (Lab A), Marcol oil 82 (Lab B), and decane (Lab C). Additional measures were taken to improve sampling, e.g. Lab B used a floating piston to stabilize the specimen during drilling by the application of a small axial force. The other two labs have the technical means to apply the same procedure but did not consider it necessary for Opalinus Clay. The material was never put in contact with water during the extraction process to avoid possible alteration. Before testing, the prepared specimens were submerged in the cooling fluids for preservation (to minimize water evaporation). For Lab C, the specimens were removed from the hydrocarbon fluid (decane) and placed into controlled humidity vacuum desiccators for three to four weeks, prior to testing. This is explained further in the next section.

To assess material heterogeneity of the cores, basic properties and mineralogical composition of tested specimens were also analysed (Table 2). Bulk density (ρ_b) was computed from specimen weight and dimensions when placed into the rig. Specimen volume was measured from calliper measurements of the specimens' height and diameter. Water content (w) was established by oven-drying (at 105 °C until constant weight) the specimen after testing and dividing the difference between initial weight and dry weight by the dry weight. Grain density (ρ_s) and bulk mineralogy (by quantitative X-ray diffraction, QXRD) were evaluated also on tested specimens, but by a contractor external to the benchmark study (University of Berne, RWI group) to avoid analytical discrepancies. In the case of the samples tested at Lab C, only one set of measurements of grain density and bulk mineralogy was performed on a slightly larger specimen compared to those used for triaxial testing to provide enough material for robust analyses. Based on the XCT scans this measurement can be considered representative for all the tested specimens. In the case of Lab

B, cylindrical specimens longer than the target height were extracted from the core; the excess material was then cut after the extraction and used for the determination of the water content and bulk density. Porosity (n) was calculated from the densities and the water content, as well as the degree of saturation of the specimens. All specimens exhibited a high degree of saturation (>90%), which indicates good preservation of the core samples, and adequate methodologies adopted for specimen extraction and preparation. This finding is also supported by measurements of total suction, which is the sum of the matric and osmotic suction,[14] of both crushed (Lab B) and intact samples (Lab C), yielding values of relative humidity around 94%–95%.

Regarding the mineralogical composition, the results in Table 2 confirm the very low heterogeneity observed in the basic properties among the specimens extracted from one core, and also between the different cores used by the different laboratories. The average mineralogical composition of all examined test specimens is illustrated in Fig. 2. The results of the mineralogical analysis are also consistent with previous studies of Opalinus Clay from the shaly facies in Mont Terri.[24,30,31]

2.3. Testing procedures

Two different testing procedures were adopted to perform undrained triaxial tests. They are named in the following "conventional" and "alternative" procedure, respectively, and abbreviated in the following as Conv-procedure and Alt-procedure. The key difference between the two procedures is the fact, that in the Alt-procedure the specimen is never brought in contact with a synthetic pore fluid. This requires a special methodology to achieve sample saturation briefly explained below. A schematic overview of the two experimental procedures is presented in Fig. 3. The graphs refer just to the phases before the shearing.

The conventional procedure was used by Lab A and Lab B, and it initiated by applying an isotropic total stress (0.5–1 MPa) to

Table 2
Overview of the basic properties and mineralogy of the tested specimens (before testing). Bulk mineralogy was evaluated by QXRD (RWI, University of Bern).

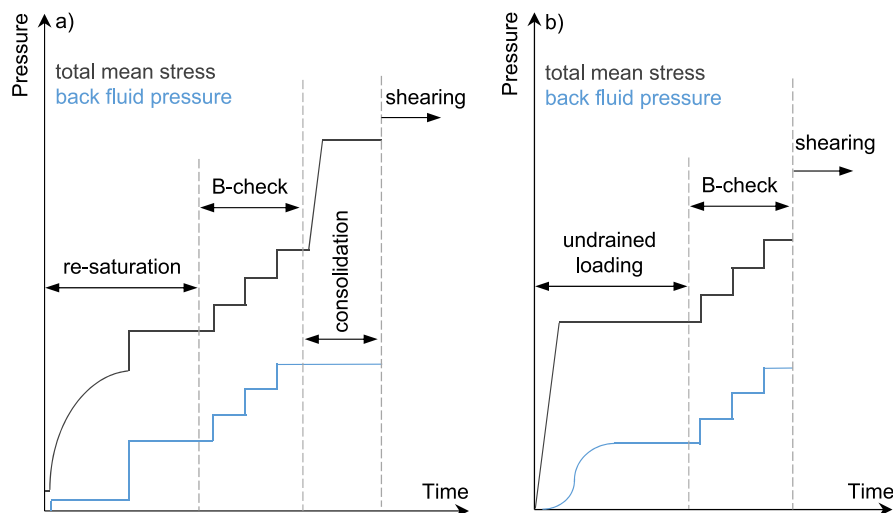|	Test ID	ρ_s [g/cc]	ρ_b [g/cc]	w [%]	n [%]	Quartz [wt.%]	Calcite [wt.%]	Clay [wt.%]
Lab A BGC2_31	AS4	2.692	2.407	6.8	16	19	13	58
	AS10a	2.691	2.391	7.1	17	18	6	64
	AS10b	–	2.410	6.9	–	–	–	–
	AS16	2.688	2.412	6.6	16	17	9	60
	AP12	2.695	2.404	6.9	17	18	10	62
Lab B BGC2_34	BS4	2.684	2.480	5.8	13	18	8	65
	BS10	2.683	2.430	6.7	15	19	7	67
	BS16	2.674	2.440	6.6	14	20	6	64
	BP4	2.692	2.420	7.0	16	13	9	71
Lab C BGC2_29	CS7	2.692	2.433	6.8	15			
	CS17	2.692	2.440	6.6	15	17	7	62
	CP9	2.692	2.407	7.1	17			
	CP17	2.692	2.441	7.0	15			
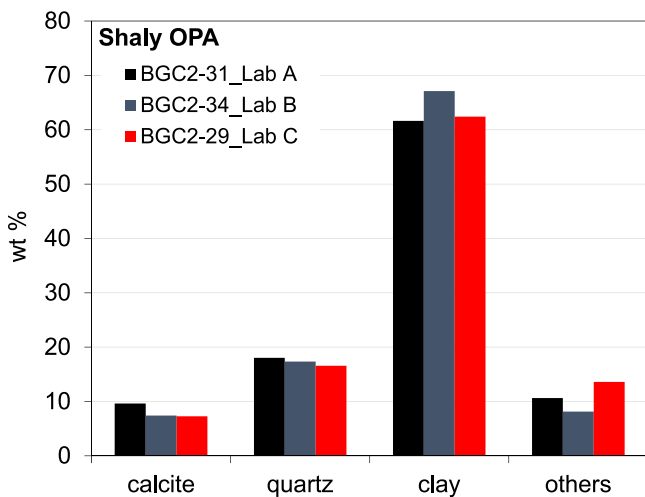
Fig. 2. Average mineralogical composition of the tested specimens grouped by cores.

the specimen to ensure good contact between the bases of the set-up and the specimen. The saturation of the specimen was then performed at constant volume to avoid possible swelling of the specimen. The specimens were initially put in contact with the fluid at the two bases, where a fluid back pressure of 100 kPa was applied in the drainage lines connecting the specimen with fluid pressure system of the apparatuses. This process progressively increases the saturation of the specimens or, in case of full saturation of the material, causes a decrease of matric suction generated during the extraction. These mechanisms are responsible for an expansion of the specimens if not properly confined; therefore, to keep the volume of the tested specimens constant, the axial and the radial stresses were independently increased as soon as expansion deformations were detected by the transducers. Conversely, this procedure allowed the determination of the axial and radial swelling pressures, respectively. This procedure is fundamental to ensure that a minimum effective stress is maintained to avoid possible damage of the specimen from volume expansion. It is noted that after extraction from the ground, the cores exhibited high effective stresses at all times due to the generation of negative pore water pressure in the pore space (i.e. matric suction). This is indicated not only by theoretical considerations, but also by the total suction measurements on initial core material and the calculated degree of saturation of the specimen (see above), as well as the swelling pressures measured during the saturation process.

Once the process stabilized, the confining stress was set equal to the axial stress and the fluid back pressure was increased to 2 MPa to dissolve possible air bubbles still remaining in the pore space[27] and the total stresses were also increased to keep the effective stress constant (Fig. 4). The assessment of the specimens' saturation was carried out by measuring the Skempton's B coefficient.[32] Three isotropic undrained loading steps (1 MPa

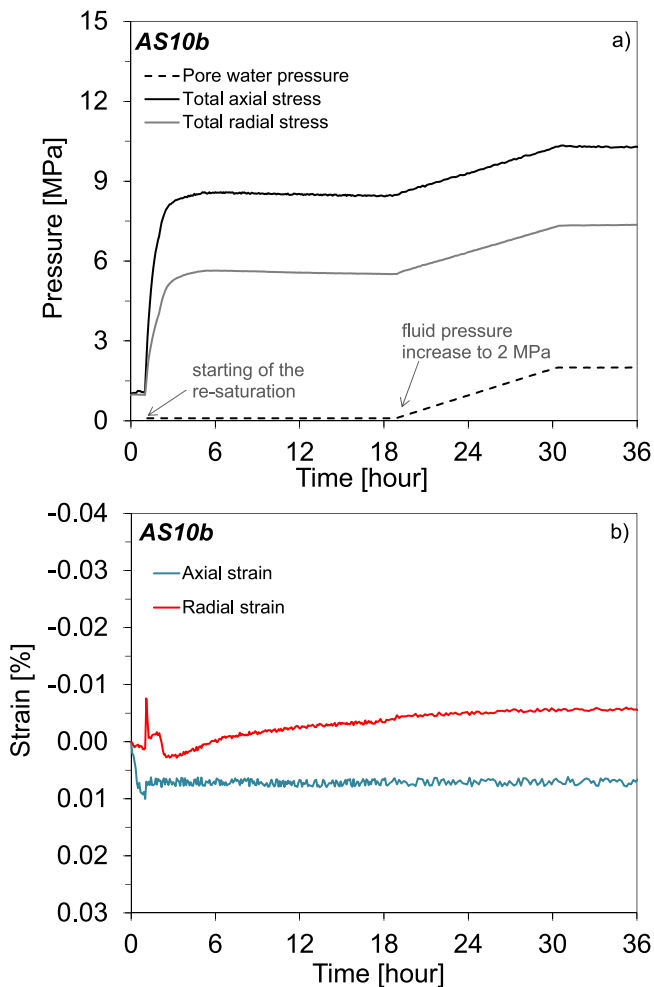**Fig. 3.** Schematic concept of the two experimental procedures: (a) conventional, (b) alternative.

Fig. 4. Example of saturation phase for the test AS10b (Lab A) performed with the conventional procedure.

procedure can avoid the direct injection of the external synthetic fluid to perform the saturation process. Instead, it exposes the specimens to different relative humidity values (between 96% and 98% for this specific study) in desiccators before testing to achieve different fluid saturation conditions. As a precautionary measure, specimens equilibrated at 98% relative humidity were inserted into a porous hard-plastic cage to prevent potential swelling of the material and allow the water exchange through the vapour phase. The cage prevents the swelling in the axial direction. Due to the high initial fluid saturation (>90%), which corresponds to values of relative humidity similar to those adopted for the equalization process (96%–98%), the swelling of the specimens during the equalization to the imposed relative humidity was negligible and it did not generate any issue in removing the specimens from the cage. The water contents presented in Table 2 refer to the specimens after the equalization in the desiccators. The specimens were then mounted into the rig; in this phase, the specimen was in contact with a very small amount of de-aired inert fluid (0.4 ml) used to fill the drainage lines. Then, an initial undrained isotropic loading was carried out until an increase of the fluid pressure was detected. During this phase, the fluid in the voids of the specimen is expected to flow out avoiding the penetration of the fluid in the drainage lines. The loading of the specimen was carried out until the achievement of a target pore fluid pressure (2 MPa). The measurement of the Skempton's B coefficient was then performed with the same protocol adopted for the Conv-procedure. To avoid exposure to a synthetic pore fluid in this particular study, drained consolidation was not applied, although it can also be executed if necessary. Therefore, the effective mean stress at the start of the shearing phase differs slightly from the starting values of the Conv-procedure. The shear phase was then executed as in the Conv-procedure at a constant axial strain rate and including two unloading–reloading cycles before and after failure of the specimens in most tests.

All the laboratories used accurate systems to monitor the specimens' deformations during the tests. All the transducers were placed inside the rigs and in direct contact with the specimens to avoid the influence of the apparatus's compliance during the application of the mechanical stresses. Lab A adopted two axial and two radial LVDTs. The two radial LVDTs are positioned at the lower and upper third point of the specimen, and they are oriented 90° apart. The internal local measurement of vertical strain is then obtained by recording the change in distance between the two horizontal strain sensors by two axial LVDTs. Lab B used three LVDTs for the axial displacement and two strain-gauged cantilevers at mid-height of the specimen for the radial displacement. Lab C implemented a system composed of eight strain-gauged cantilevers. This system allows the evaluation of the strains, both axial and radial, from the bending of the cantilevers induced by the displacements experienced by the specimen. Four cantilevers were used for the measurement of the axial strain and four more measured the orthogonal diameter changes. In the case of specimens tested parallel to bedding (P-tests), the configurations adopted by the laboratories allow the evaluation of the radial strain in the directions both perpendicular and parallel to bedding. Regarding the measurement system of the radial strain, for the Lab A and Lab B the stems are brought through the sleeve and put in direct contact with the specimen, while for the Lab C the stems are in contact with the sleeve. Additional details related to the testing layouts can be found in Refs. 20, 22, 34, 35. The accuracy and efficiency of these systems were carefully assessed with calibration tests performed on a synthetic material (peek). All the calibration tests were performed at a total confining stress of 10 MPa and included three loading–unloading cycles carried out up to a deviatoric stress equal to 10 MPa. The values of the elastic properties obtained by the three

stress increase for each of them) were usually performed in the tests. The B coefficient was calculated as the ratio between the measured increase of the pore fluid pressure (Δu) and the applied increase of the total mean stress (Δp). At the end of the last measurement, the pore fluid pressure was set equal to 5 MPa if this target value was not reached during the three loading steps before. Drained consolidation of the specimen to the target consolidation stress (p'_{in}) was then performed. The pore fluid pressure was kept constant to 5 MPa during consolidation and the consolidation coefficient was determined for the estimation of the appropriate loading rate during the shear phase (see below). The final phase of the test was the shearing of the specimens at constant axial strain rate until specimen's failure and achievement of the ultimate condition (post-peak). Peak was defined as the maximum deviator stress experienced by the specimens. Unloading–reloading cycles were also carried out before and after peak with an axial strain amplitude of 0.001. The stress variation during these cycles was applied to the specimen with same axial strain rate adopted for the main shearing phase. All the tests performed with the conventional procedure used a synthetic pore fluid prepared according to Ref. 33. The synthetic pore fluid was composed of demineralized water and different salts with the following concentration: 6.7356 g/l NaCl, 0.0456 g/l NaHCO$_3$, 1.7510 g/l CaCl$_2$ 2H$_2$O, 0.1902 g/l KCl, 1.8635 g/l MgCl$_2$ 6H$_2$O and 3.4089 g/l Na$_2$SO$_4$.

The Alt-procedure was used by Lab C, and examples of this experimental procedure can be found in Refs. 20, 22, 26. This

Table 3
Results of the performed calibration tests: Young's modulus and Poisson's ratio measured during the different cycles.

Lab A			Lab B			Lab C		
Cycle	E [GPa]	ν [–]	Cycle	E [GPa]	ν [–]	Cycle	E [GPa]	ν [–]
1	4.3	0.41	1	4.4	0.44	1	4.3	0.43
2	4.3	0.42	2	4.4	0.43	2	4.4	0.45
3	4.3	0.42	3	4.4	0.43	3	4.3	0.45

laboratories are summarized in Table 3, and they demonstrated the good capability of the testing set-ups in providing robust measurements.

A summary of the strain rates adopted by the three laboratories to perform the undrained shearing phase is presented in Table 4 for the S-tests and in Table 5 for the P-tests. The selection of the appropriate strain rates is fundamental for equilibration of the pore fluid pressure across the specimen for robust determination of the mechanical properties in terms of effective stresses. This aspect was widely investigated in recent works on shales where the methodologies proposed in Refs. 36, 37 were considered for the estimation of the strain rate. The key factors required for the theoretical estimation of allowable strain rate are the size of the tested specimens, the coefficient of consolidation (c_v), the drainage configuration, and the estimated axial strain to failure. The size of the specimens has a pronounced effect on the strain rate, and for this reason the laboratories used sizes smaller than conventional as mentioned above. The evaluation of the c_v coefficient was performed during the consolidation phase of the tests carried out with the conventional procedure (Lab A and Lab B), yielding a value of approximately 2.5×10^{-9} m^2/s in the stress range relevant for the compression tests. This value is also consistent with previous findings on the same material.[31] All the laboratories used lateral drains in order to allow faster pore fluid pressure equalization in the specimens. The Lab A used four drains made of vyon (porous plastic material made of polyethylene), while the Lab B and the Lab C implemented drains made of permeable metal strips. The connectivity of the lateral drains was previously verified with specific evaluation test. According to the methodology presented in Ref. 36, a drainage coefficient of 64 and a drainage path length equal to the radius of the specimens were therefore used for the calculation. The axial strain at failure was considered to be equal to 0.01. Based on these considerations and on the different size of the specimens adopted by the laboratories, an appropriate axial strain rate for undrained loading of approximately 5×10^{-7} s^{-1} was obtained for Lab A and Lab B, and approximately 1×10^{-6} s^{-1} for Lab C, respectively. As reported in Tables 4 and 5, much lower strain rate values were however adopted for the performance of the tests; this choice was considered as a precautionary measure to ensure a correct evaluation of the pore fluid pressure also in the case of limited efficiency of the side drains caused by the elevated confining stress. In particular, Lab A and Lab C used strain rates approximately one order of magnitude lower than the theoretical value, while Lab B adopted strain rates approximately 2–3 times lower.

All laboratories performed the undrained tests with very small dead volumes of the fluid pressure system (≤ 2.2 ml) to minimize effects of system compliance for the measurement of fluid pressure. This is relevant not only during the shearing phase, but also for the assessment of the Skempton's B coefficient. In addition, a reliable assessment of the fluid pressure requires the minimization of temperature fluctuations. The tests were performed at room temperature, and measures were taken to reduce and control the temperature variations typically within 1 °C.

3. Results

This section presents selected results of the performed tests as representative examples. Summary plots of all test results are introduced and discussed in Section 4.

The results are illustrated referring to the effective mean stress (p′) and deviator stress (q) as follows:

$$p' = \frac{\sigma_a' + 2\sigma_r'}{3}$$

$$q = \sigma_a' - \sigma_r'$$

where σ_a' and σ_r' are the effective axial and radial stress during the loading of the specimens. The adopted convention for the strains (axial ε_a, radial ε_r, volumetric ε_{vol}) is positive for compression and negative for extension. The maximum value of q during a test sequence is denoted as q_f (for «failure»), as all tests exhibited strain-weakening. Accordingly, the value of p′ at q_f is referred to as p'_f (cf. Tables 4 and 5); in the tables the deviator stress and mean effective stress are defined also for the post-peak condition achieved after failure (i.e. constant deviator stress) as q_{pp} and p'_{pp}.

To evaluate the hydro-mechanical response of the tested specimens, the pore pressure parameter AB[32] was also considered:

$$AB = \frac{\Delta u_w}{\Delta q}$$

where Δu_w is the variation of the pore fluid pressure and Δq is the variation of deviator stress, both measured from the beginning of deviatoric loading.

3.1. Saturation phase

Establishing specimen saturation in the rig was particularly delicate in the case of the Conv-procedure where volume expansion of the specimens by direct contact with the synthetic fluid had to be counteracted by simultaneously raising axial and radial stress. An example of this initial phase of the tests is presented in Fig. 4 (test AS10b performed by Lab A). The graphs (a) and (b) illustrate the evolution in time of the stresses (axial and radial) and the fluid pressure, and the strains (axial and radial). The graph (a) in Fig. 4 shows the initial low isotropic stress acting on the specimens (1 MPa). Then a small fluid pressure was applied (about 80 kPa) to carry out the re-saturation process. Due to the imposed constant volume conditions, the development of the swelling stresses was observed. The graph (b) in Fig. 4 highlights the evolution in time of the recorded deformations. The strains were indeed extremely small ($\leq 0.01\%$) and demonstrated the good capability in limiting the expansion of the specimens in both directions. A slight expansion was observed in the radial direction, and it stabilized after about 18 h. The development of the swelling pressure in graph (a) shows a more pronounced stress in the axial direction (perpendicular to the bedding) than in the radial direction (8.5 MPa against 5.6 MPa). Once the stresses and strains stabilized, the fluid pressure was raised to 2 MPa to enhance the saturation process (the two stresses were also raised to keep the effective stress constant). The small strains experienced by the specimen demonstrated that the procedure was suitable to properly re-saturate the specimens without inducing relevant volumetric deformations that could have altered the porosity of the specimens and ultimately its mechanical response.

The saturation phase of the tests included also the measurement of the Skempton's B coefficient. As presented in Section 2.3, the measurement of the Skempton's B coefficient was performed in steps by increasing the total mean stress in undrained conditions. An example of this phase is presented in Fig. 5 (test CS7, Lab C). The specimen was here loaded in three steps, with an increase

Table 4
Summary of the testing results of all the performed S-tests.

Test ID	Strain rate [s^{-1}]	p$'_{in}$ [MPa]	B [–]	E$_{uc}$ [GPa]	ν [–]	q$_f$ [MPa]	p$'_f$ [MPa]	q$_{pp}$ [MPa]	p$'_{pp}$ [MPa]
AS4	4.8 × 10^{-8}	4.0	0.66	3.1	0.38	8.4	5.3	7.1	6.1
AS10a	4.8 × 10^{-8}	10.0	0.86	4.0	0.49	15.4	11.8	10.0	12.8
AS10b	9.7 × 10^{-8}	10.0	0.85	4.7	0.32	14.3	10.5	9.3	10.7
AS16	4.8 × 10^{-8}	16.0	0.60	5.6	0.45	18.6	16.2	15.3	16.9
BS4	2 × 10^{-7}	4.0	0.96	2.7	0.39	9.8	5.5	6.7	7.1
BS10	2 × 10^{-7}	10.0	0.88	4.0	0.39	14.3	9.4	8.1	9.7
BS16	3 × 10^{-7}	16.0	0.97	5.1	0.39	21.6	16.5	13.3	17.3
CS7	2 × 10^{-7}	7.0	0.95	3.3	0.53	13.2	8.3	7.8	8.7
CS17	1 × 10^{-7}	16.8	0.95	4.8	0.57	20.9	17.3	12.5	15.5

Table 5
Summary of the testing results of all the performed P-tests.

Test ID	Strain rate [s^{-1}]	p$'_{in}$ [MPa]	B [–]	E$_{uc}$ [GPa]	ν$_{\parallel}$ [–]	ν$_{\perp}$ [–]	q$_f$ [MPa]	p$'_f$ [MPa]	q$_{pp}$ [MPa]	p$'_{pp}$ [MPa]
AP12	4.8 × 10^{-8}	10.0	0.77	10.7	0.21	0.73	26.0	18.6	13.0	16.1
BP4	1 × 10^{-7}	4.0	0.94	7.8	0.22	0.66	16.4	8.7	9.2	7.0
CP9	2 × 10^{-7}	8.6	0.98	8.6	0.35	0.92	22.1	13.5	10.2	10.2
CP17	2 × 10^{-7}	16.6	0.95	–	–	–	31.6	23.8	16.0	18.5
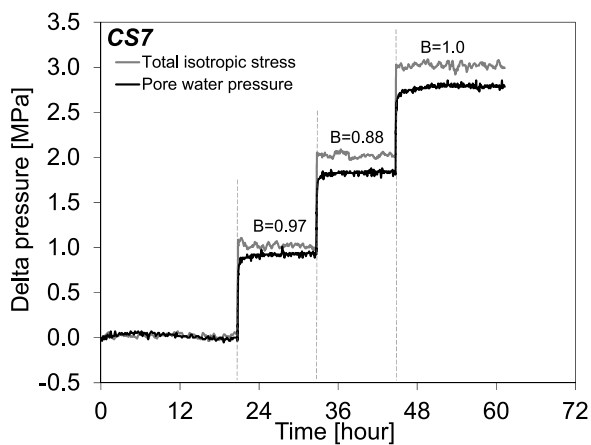
Fig. 5. Example of Skempton's B coefficient measurement for the test CS7 (Lab C).

of the total isotropic stress of 1 MPa. The considered fluid pressure for the calculation of the B coefficient was evaluated when a good stabilization was achieved during each step; this condition was usually observed after few hours from the stress application and it is consistent with the method reported in Ref. 22. When a stabilization was not observed (see Section 4.1), the fluid pressure was evaluated after two hours from the starting of the undrained loading. The three obtained values of the B coefficient were within the range ±0.06, with an average value of 0.95. At each step, the B coefficient was calculated using the maximum measured fluid pressure. This result supported the assumption that the specimens achieved a stable saturated condition. Similar responses were observed also in the other tests, and a summary of all the B coefficients measured in the performed tests is presented in Section 4.1.

3.2. Shearing behaviour

3.2.1. S-tests

A representative example of test results for the shear phase of an S-test is provided in Fig. 6 for test BS10, loaded from an initial effective mean stress of 10 MPa. Different graphs considering the stresses, strains, pore fluid pressure variation, and AB parameter allowed a comprehensive diagnostic interpretation of the material response. The maximum values of deviator stress

(max q, equal to q$_f$), pore fluid pressure change (max Δu$_w$), and AB parameter (max AB) are also indicated in each graph. These points allowed the subdivision of the shearing in three principal stages (cf. Ref. 22): (i) from the starting of the shearing to the max AB point, (ii) from max AB point to the max Δu$_w$ point, and (iii) from the max Δu$_w$ point to the max q point. The graphs also illustrate the two unloading–reloading cycles performed before and after the achievement of the maximum deviator stress for the evaluation of the elastic properties of the specimen (cf. Section 3.3).

The graph (a) in Fig. 6 shows the relationship between the axial stress and the axial strain and highlights the nonlinear response of the tested specimen. This nonlinearity was related to the elasto-plastic hardening behaviour of the material before the achievement of the maximum deviator stress. This feature was well highlighted by irreversible axial deformation exhibited during the unloading phase of the stress cycle performed before the failure of the specimens. A Similar nonlinear response was also observed in the radial direction in the graph (d) (Fig. 6); the graph only shows the deformation up the peak stress because after the failure of the specimen the local measurement of the radial strain could not be considered anymore representative of the real material's response. Once the maximum deviator stress is achieved, a rapid stress decrease was experienced by the specimen. This stress drop was interpreted as a brittle response of the tested specimen. The shearing of the specimen then continued until the achievement of the post-peak (or ultimate) condition where constant deviator stress was exhibited. The achievement of the maximum deviator stress was considered to be representative of the specimen's failure. The failure can be related to the development of a discrete shear fracture across the specimen as evidenced by post-testing visual inspection (Fig. 7). This observation is representative for all tests. The different colour of the specimens in the picture is related to the different lighting conditions in the laboratories and not to the mineralogical composition.

The max AB value is evaluated in graph (f) in Fig. 6 and it is manifested in graphs (c) (fluid pressure versus axial strain) and (e) (deviatoric stress versus fluid pressure) by progressive deviation from linearity above this value. At the deviator stress corresponding to the max AB value, the rate of fluid pressure increase reaches a maximum. Fluid pressure is still increasing with additional loading, but a lower rate per increment in deviator stress or strain. Both graphs (c) and (e) also clearly illustrate that the maximum value of fluid pressure (max Δu$_w$) was achieved well before the maximum deviator stress. This aspect indicates
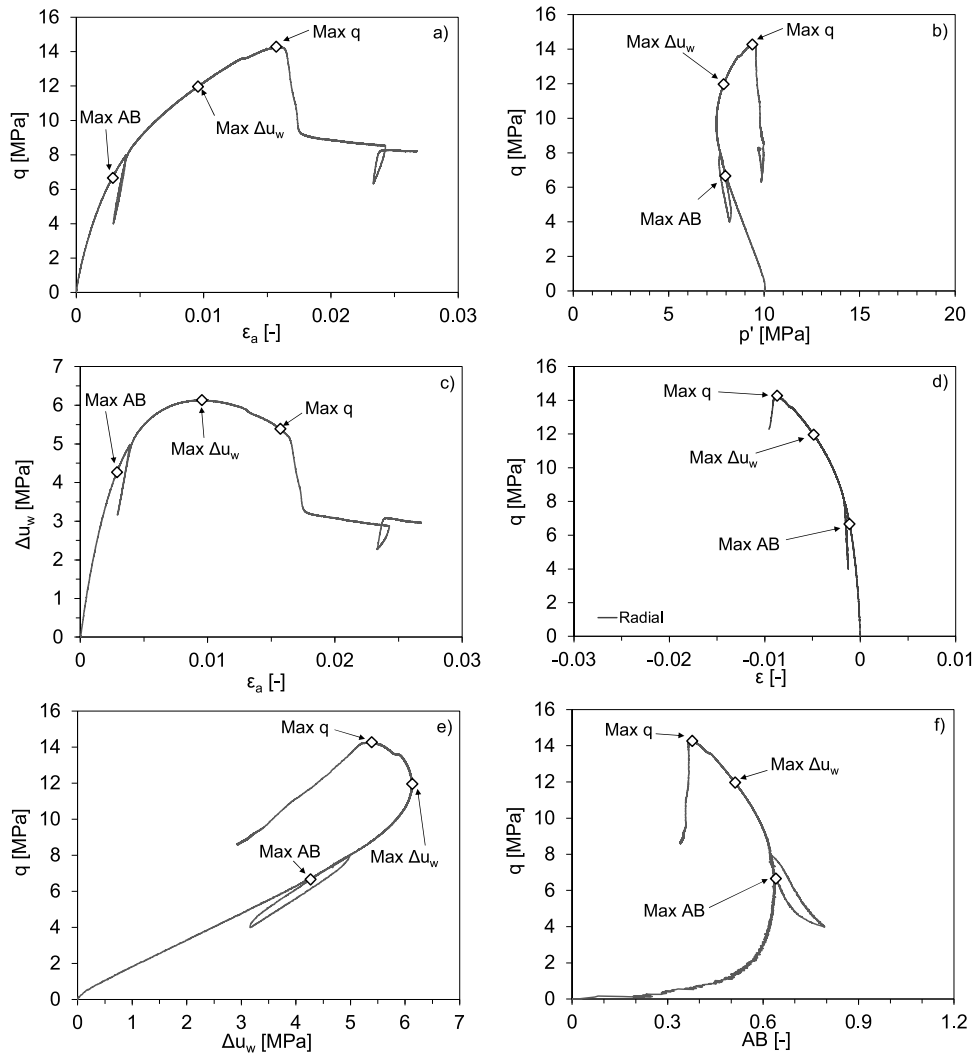
Fig. 6. Example of testing result for an S-test performed at $p'_{in} = 10$ MPa (BS10, Lab B).
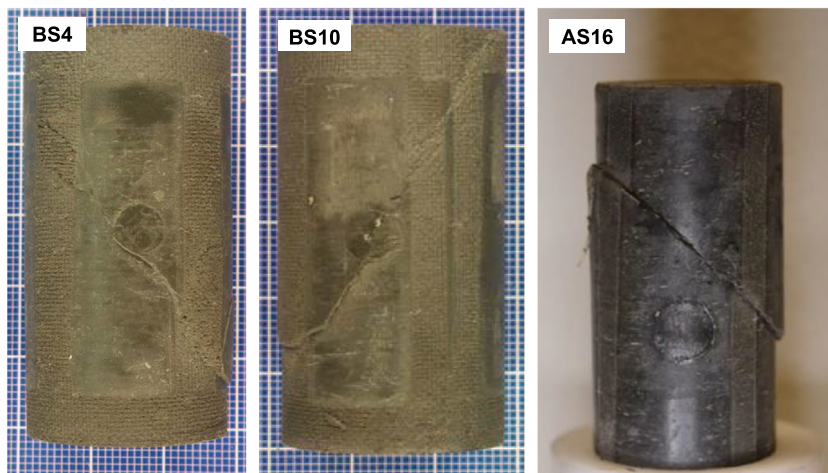

Fig. 7. Example of specimens after testing (S-tests) showing the presence of a discrete fracture.

that failure of the specimen was associated to a dilation mechanism and it can be related to the generation of the shear fracture. These features suggested that the max AB point can provide an indication of the onset of the failure process in the material. This

evolution of the fluid pressure during shearing affected significantly the effective stress path. The graph (b) in Fig. 6 illustrates the relationship between the deviator stress and the effective mean stress. The evolution was marked by an initial decrease
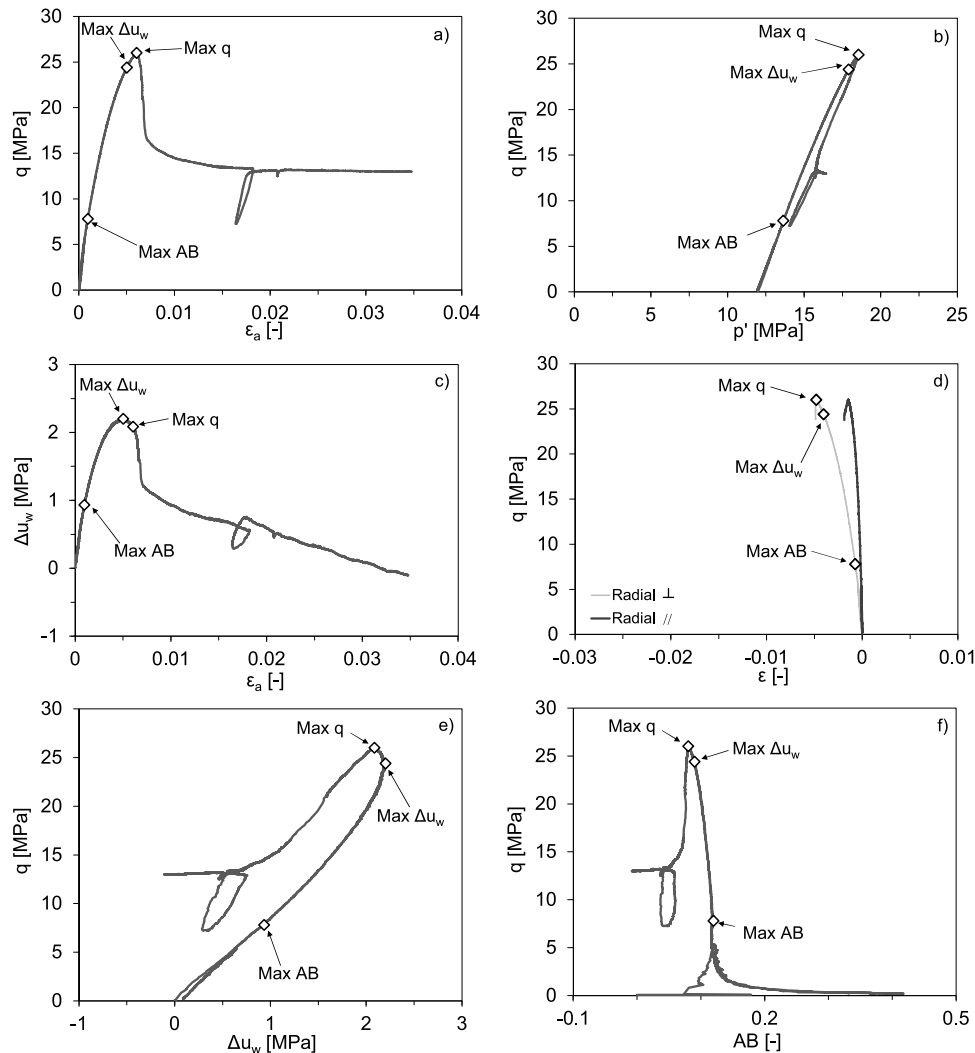
Fig. 8. Example of testing result for a P-test performed at p'_{in} = 12 MPa (AP12).

of the effective mean stress, followed by an increase up to the achievement of the maximum deviator stress.

3.2.2. P-tests

A representative example of test results for the shear phase of a P-test is provided in Fig. 8 for test AP12, loaded from an initial effective mean stress of 12 MPa, i.e. similar to the S-test in Fig. 6. A very different hydro-mechanical response was exhibited in the P-tests with respect to S-tests. In contrast to S-tests, no irreversible deformation is observed in an unloading–reloading cycle in comparison with initial loading. The axial strain to failure was less than 50% of the strain in the S-test at similar effective stress. The maximum value of the pore fluid pressure variation experienced by the specimen was about 2 MPa, significantly lower than in the S-test (about 6 MPa in the graph (c) of Fig. 6). The lack of significant additional pore fluid pressure generated during loading means that pore pressure was not sufficient to induce a significant reduction of the effective mean stress as in the case of S-tests.

The max AB cannot be identified with confidence as in the S-test (Fig. 6f). Therefore, the use of the max AB point to evaluate the onset of the plastic behaviour in P-tests must be considered with caution. A key aspect is that the pore fluid pressure reaches a maximum at almost the maximum deviator stress. This means that the fluid pressure increased almost up the failure of the

specimen, and the rate of increase changed only significantly shortly before reaching the maximum value.

After testing, the inspection of the specimens highlighted the presence of a clear shear fracture as in S-tests (Fig. 9). The fracture was always crossing the bedding planes of the specimens and axial splitting was never observed. In particular, the shear fractures showed a higher inclination with respect to the radial direction compared to the specimens in S-tests, indicating a slight influence of the bedding orientation in the testing configuration.

3.3. Elastic response

The elastic response of the tested specimens was evaluated on the performed unloading–reloading cycles during the shearing phase before and after achieving q_f. All the computed parameters (elastic moduli and Poisson's ratio) refer to undrained conditions considering linear anisotropic elasticity.

The unloading phase of the cycles allowed the typical determination of the secant undrained elastic modulus (E_{uc}), which was computed as the ratio between the axial stress interval ($\Delta\sigma_a$) and the corresponding axial strain variation experienced by the specimen ($\Delta\varepsilon_a$), for both the pre- and the post-peak response, in spite of the presence of clear fracture planes in the latter case. The stress–strain curve is found to be significantly non-linear, meaning that a greater unloading increment will result in lower
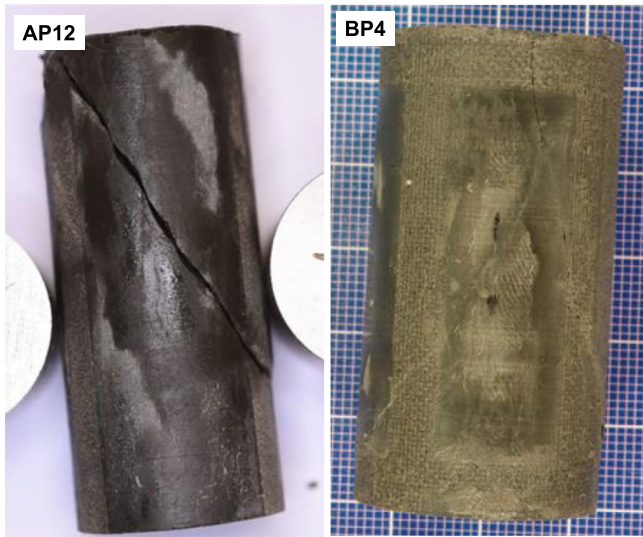
Fig. 9. Examples of specimen after testing (P-tests) showing the presence of one (left) or multiple (right) distinct fractures.
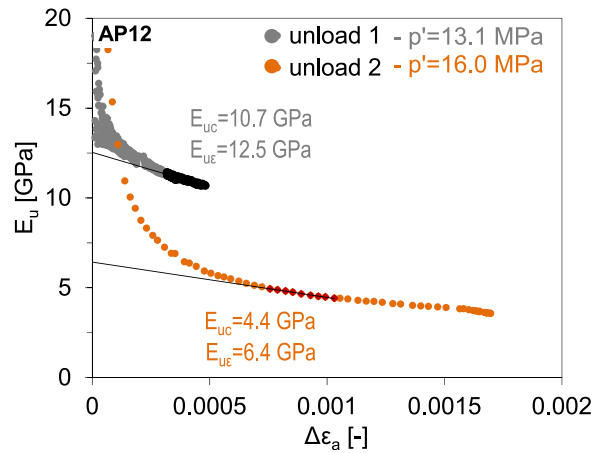

Fig. 11. Undrained elastic moduli measured on the unloading phase of the cycles performed before and after specimen's failure in the P-test AP12 (Lab A).

apparent E_{uc} value. Therefore, small-strain moduli ($E_{u\varepsilon}$) were also evaluated from the stress cycles according to the procedure by Ref. 38 and applied with minor modification for the Opalinus Clay by Ref. 22. An example of its determination and comparison with the secant moduli E_{uc} is presented in Fig. 10 for the S-tests BS16 (Lab B) and AS10a (Lab A). The graph shows the evolution of the secant modulus with the axial strain during the unloading phase of the cycles performed before (*cycle pre-peak or unload 1*) and after (*cycle post-peak or unload 2*) failure (q_f). A clear nonlinear decrease of the stiffness was observed as the axial strain range used for the calculation increased, which reflected the nonlinearity of the material's response. The graphs highlighted the strain dependency of elastic stiffness where higher small strain values ($E_{u\varepsilon}$) with respect to secant values (E_{uc}) were systematically observed. The importance of the axial strain range adopted to perform unloading–reloading cycles is illustrated in the graph (b) of Fig. 10, where different axial strain ranges led to different moduli. Generally, larger axial strain ranges lead to lower moduli (both E_{uc} and $E_{u\varepsilon}$). As an example, the values of E_{uc} computed on the unload 2 interval at an axial strain of 0.001 yields 2.8 GPa, while at a strain of 0.0037 (end of the unloading) it yields a value 1.6 GPa. For this reason, an axial strain range of 0.001 was selected in most of the performed tests for both cycles before and after the peak stress in order to have a consistent evaluation of the elastic parameters. Indeed, larger strain interval

would have led to additional variations of the moduli negligible compared to the overall range exhibited by the material during the unloading. When higher strain intervals were used (as for the *unload 2* in the graph (b) of Fig. 10), the moduli were evaluated for the target axial strain of 0.001.

Fig. 11 shows an example for the P-test AP12 (Lab A). A trend similar to that observed for the S-test in Fig. 10 is exhibited also in this case. The graph highlights the higher stiffness of the material with respect to the results in the graph (a) of Fig. 10. Note that the initial effective mean stress in the two tests BS16 and AP12 is different by 6 MPa, but the effective mean stress at the start of *unload 1* is comparable (13.1 MPa and 13.3 MPa, respectively). This result demonstrates the anisotropic elastic response of Opalinus Clay. Moreover, the graphs in Figs. 10 and 11 highlighted also systematic lower values of the moduli measured on the cycle performed after the peak stress (*unload 2*). This highlights the importance of avoiding specimens' damage to derive robust elastic parameters representative of the intact material.

In terms of radial response, the relationship between axial and radial strains (Fig. 12) during the unloading phase of the cycles performed before the achievement of the maximum deviatoric stress was used for the assessment of the undrained Poisson's ratio (ν_u). The graph (a) in Fig. 12 shows an example of the relationship between the two strains during the unloading phase of the cycles of the S-test BS16. For the determination of the undrained Poisson's ratio, nearly perfect linear relationship over the entire unloading phase was observed between radial and axial strains. Similar linear trends were observed also for the other S
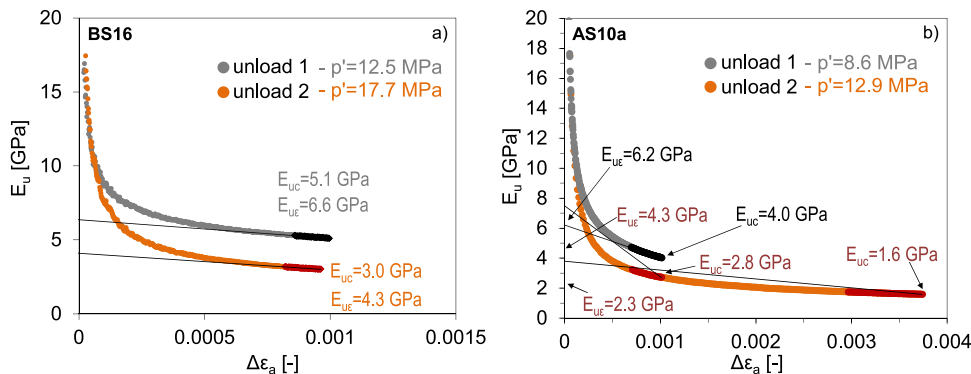

Fig. 10. Undrained elastic moduli measured on the unloading phase of the cycles performed before and after specimen's failure in the S-tests BS16 in graph (a), and AS10a in the graph (b).
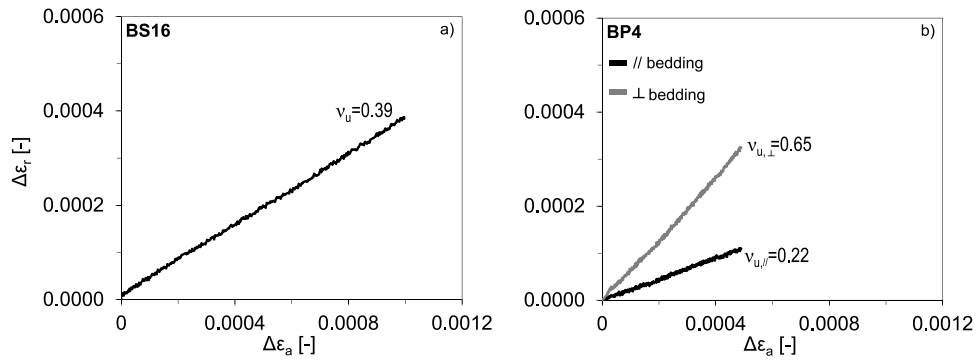
Fig. 12. Relationship between axial and radial strains during the unloading phase of the pre-peak cycle for: (a) S-test (BS16), and (b) P-test (BP4).

tests. The analysis of the radial response in the P-tests revealed a significant anisotropic response of the tested specimens. Indeed, the presence of the bedding planes in the axial direction influenced significantly the response of the specimens in the two orthogonal directions in the horizontal planes; in particular, a higher strain in the direction perpendicular to bedding than in the direction parallel to bedding was always observed. An example of this behaviour (for the test BP4) is presented in the graph (b) of Fig. 12. Also in this case a linear relationship was observed for both radial strains, and a value of undrained Poisson's ratio could be computed for each direction (perpendicular $\nu_{u,\perp}$ and parallel $\nu_{u,\parallel}$ to bedding). This feature of the Opalinus Clay behaviour highlighted the importance of measuring the radial deformations in the two orthogonal directions, one aligned with the bedding plane, for a proper evaluation of the elastic response during P-tests.

4. Discussion and comparison

In this section a comparison of the benchmark test results is presented in summary graphs. The comparison first focuses on the saturation phase, then the elastic response, and finally the shearing behaviour. Moreover, Tables 4 and 5 summarize the test conditions and results for both S- and P-tests, respectively.

4.1. Saturation phase

A summary of the Skempton's B-coefficients measured by the different laboratories is provided in Fig. 13. The values are reported against the effective mean stress acting on the specimens. As three steps were usually performed in each test to evaluate the B coefficient, the average of the three measurements is presented in Fig. 13, and in Tables 4 and 5. Values higher than 0.8 were systematically obtained by the Lab B and Lab C, and they indicated a good consistency of the experimental results. Differences between the values measured at the different steps were in the range ± 0.06, suggesting that both the conventional and alternative procedure was appropriate to re-saturate the tested specimens.

Lower values were measured by Lab A, and more significantly the pore fluid pressure was decreasing with time at a rate of about 100 kPa over 24 h after the initial increase in response to the mean stress step increase of 1 MPa (Fig. 14a). A detailed calibration of the testing set-up late in the testing programme confirmed that the pressure loss occurs through dissipation across the specimen sleeve at a rate of approximately 2 to 14 kPa per hour. The nitrile rubber membrane used as sleeve was therefore replaced by a Viton membrane in test AS10b, essentially a repeat of AS10a but with the different membrane (Table 1). In this case, fluid pressure did not drop anymore after
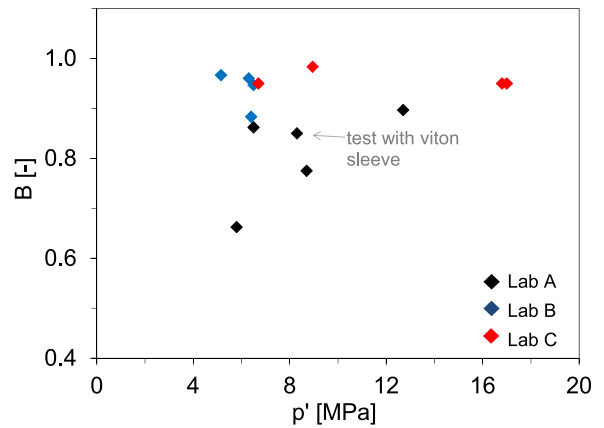

**Fig. 13.** Measured values of the Skempton's B coefficient.

a mean stress step increase (Fig. 14b). However, the low B-values exclusively measured by Lab A are difficult to be explained by fluid pressure loss across the membrane only. It may be speculated that some air may have been trapped in the system (e.g. the side drains) at the start of the Skempton-B tests, leading to greater fluctuations and lower B-values due to lower water compressibility after dissolution of air bubbles in the pore fluid. Another possible explanation could be a lower stiffness of the system (pressure transducer, tubing, filters etc.).

Test AS10b was the only one carried out by Lab A with a Viton rubber sleeve, while all the other tests were performed with nitrile rubber sleeve. The leakage across the sleeve also impacted in the development of the pore fluid pressure during the loading of the specimens in tests of Lab A, as is discussed in Section 4.3.

4.2. Elastic response

A summary of all the elastic parameters obtained from the benchmark campaign is illustrated in this section to highlight the general consistency of the results obtained by the different laboratories and validate the experimental procedures. As specified in Section 3.2, all the presented values of the elastic moduli and Poisson's ratio refer to undrained conditions and were mainly evaluated on the unloading phase of the unloading–reloading cycles before and after the maximum deviatoric stress.

The graphs in Fig. 15 summarize the different elastic moduli obtained from the S- and P-tests. The graphs show the secant moduli E_{uc} measured before (*Cycle pre-peak*) and after (*Cycle post-peak*) failure, the small strain moduli $E_{u\varepsilon}$ evaluated on the cycle before the peak stress, and the primary loading moduli E_{u0} evaluated at the beginning of the shearing of the specimens.
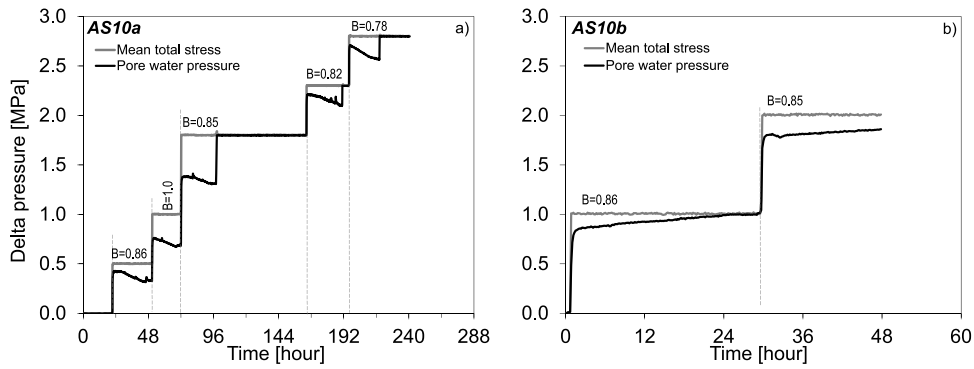
Fig. 14. Impact of different types of sleeves on the evolution of the fluid pressure during the measurements of the B coefficient for the tests (a) AS10a nitrile rubber sleeve, and (b) AS10b Viton rubber sleeve.
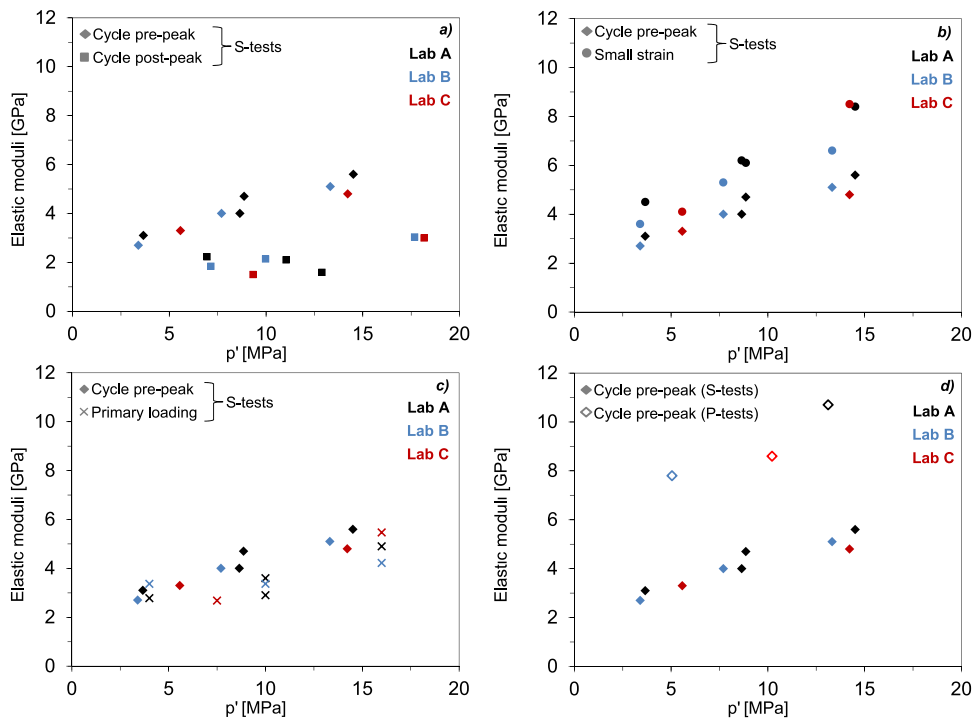
Fig. 15. Undrained elastic Young's moduli measured in the performed tests. The graphs (a), (b), and (c) illustrate a comparison of the moduli for the S-tests determined on the stress cycles before and after the peak, the primary loading, and the small strain moduli. The graph (d) shows a comparison of the moduli determined on the stress cycle before the peak between the S-tests and P-tests.

The moduli E_{uc} and $E_{u\varepsilon}$ were plotted versus the effective mean stress acting on the specimens at the starting of the unloading, while the primary loading moduli E_{u0} were plotted versus the effective mean stress acting on the specimens at the starting of the shearing. A good consistency of the values obtained by the different laboratories is observed. The following three main systematic features could be highlighted: (i) the dependence of the moduli on the mean effective stress (p′), (ii) the decrease and lack of a clear stress-dependance of the secant elastic moduli after failure of the specimens (*Cycle post-peak* are lower than *Cycle pre-peak*, graph (a) in Fig. 15), (iii) the influence of the strain range cosidered to obtain the moduli (*Small strain* moduli are greater than *Cycle pre-peak* moduli, graph (b) in Fig. 15). The elastic anisotropic response of Opalinus Clay is also highlighted in the graph (d) of Fig. 15. The specimens loaded parallel to bedding (P-tests) exhibited much greater values of the undrained elastic moduli compared to the S-tests. The anisotropy factor between 2 and 3 is consistent with findings on drained tests by 21.

Regarding the Poisson's ratio, a summary of the obtained values for the S- and P-tests is presented in Fig. 16. As for the elastic moduli, these values were plotted versus the effective mean stress acting on the specimens at the starting of the unloading phase. In the case of the S-tests, the values of ν_u were in the range between 0.30 and 0.55. It is noted that values in excess of 0.5 are plausible given the anisotropic response of Opalinus Clay, as the maximum theoretical value of 0.5 applies to linear isotropic elasticity. The following two ranges were identified for the P-tests: 0.2–0.4 for the direction parallel to bedding ($\nu_{u,\parallel}$), and 0.6–1.0 for the direction perpendicular to bedding ($\nu_{u,\perp}$). The radial anisotropic response was observed in all the P-tests carried out by the three different laboratories. Finally, the cycles carried out after the failure of the specimens were not considered for the evaluation of the Poisson's ratio, as the geometry of the failure plane affects the local measurement of the radial displacements. A summary of the key undrained elastic parameters is presented in Tables 4 and 5, where the secant values of the elastic modulus and the Poisson's ratio measured on the cycles before failure are reported.
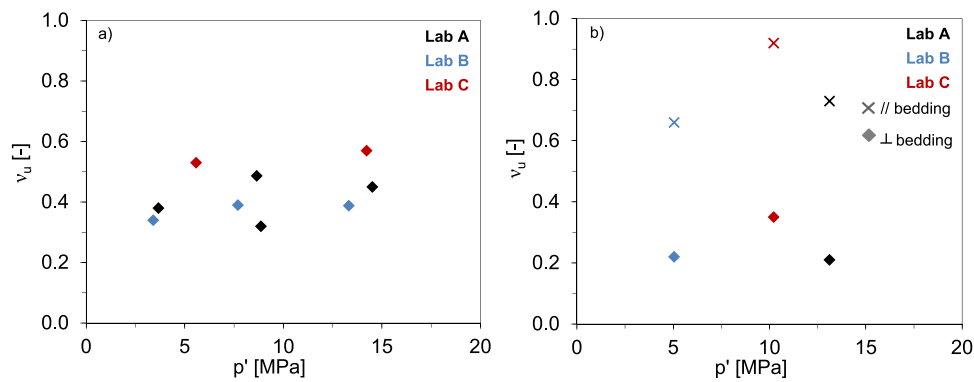
Fig. 16. Relationship between the mean effective stress and the undrained Poisson's ratio for (a) the S-tests, and (b) the P-tests.
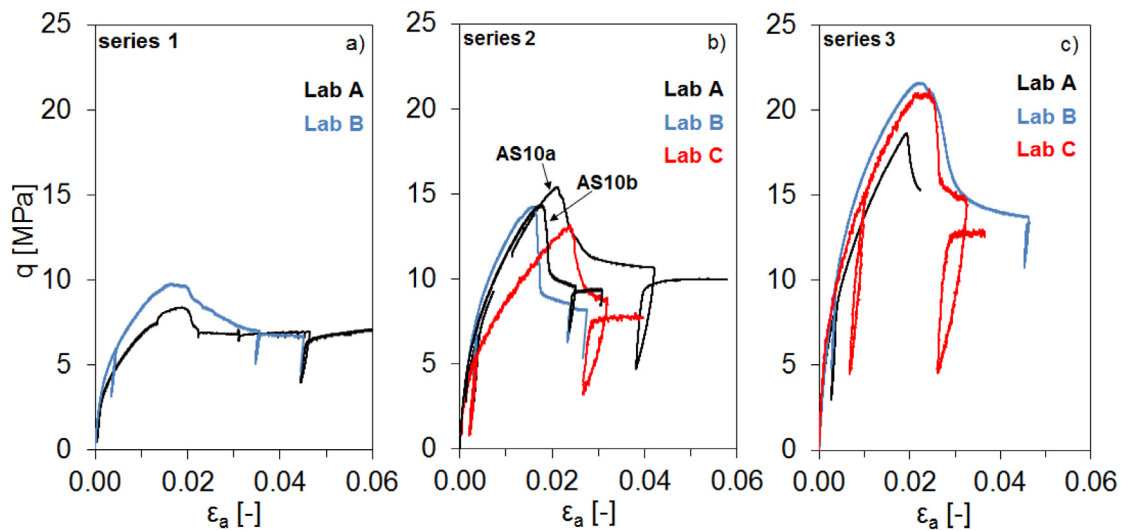

Fig. 17. Axial stress vs. axial strain for the performed S-tests. (a) Tests performed at 4 MPa of effective confining stress. (b) Tests performed at 10 MPa (Lab A and Lab B) and 7 MPa (Lab C) of effective confining stress. (c) Tests performed at 16 MPa (Lab A and Lab B) and 16.8 MPa (Lab C) of effective confining stress.

The apparent systematic difference in Poisson's ratio values among the different labs might reflect slight differences in material properties for each lab's core section, or might be due to specific combinations of specimen size, dead volume related to the drainage configuration and loading rate. As reported in Section 2.3, calibration tests (blind cross-check) using a standard peek material resulted in identical Young's modulus and Poisson's ratio results from the different labs.

4.3. Shearing behaviour

Concerning the S-tests, the three graphs in Fig. 17 show a direct comparison of the stress–strain relationships for the three series of tests performed at similar initial effective confining stresses. It is noted that for Lab C, the initial effective confining stress is slightly different (p'_{in} = 7 instead of 10 MPa, and 17 instead of 16 MPa, respectively), but the test results of Lab C are plotted at the closest effective stress levels of tests performed by the other labs (graphs b and c in Fig. 17).

Similar stress–strain responses were observed in the tests performed by the different laboratories, reaching failure at an axial strain of approximately 0.02. In particular, the graph (a) in Fig. 17 illustrates the similar response of two S-tests carried out by Lab A and Lab B, both using the conventional procedure. A good agreement between Lab A and Lab B was also observed in the graph (b) in Fig. 17 for test AS10b. The apparent lower stiffness exhibited in the test by the Lab C may largely be attributed to

the lower effective stress (cf. graph (a) in Fig. 17). Graph (c) of Fig. 17 highlights the broad consistency of the results obtained with the conventional (Lab A and Lab B) and alternative (Lab C) testing procedures for tests performed at near identical initial mean stress. The apparent lower peak strength of Lab A in Fig. 17c is discussed further below.

Probably the best overview of test results is granted when the effective stress paths (deviatoric stress versus effective mean stress) are considered. This is done for all S-tests in Fig. 18, grouped by tests from all three laboratories. All stress paths are qualitatively similar in shape, with a decrease of the effective mean stress in the initial part, followed by an increase in the second part until reaching the maximum deviatoric stress. As mentioned in the previous section, the right curvature indicated that the failure of the specimens was related to a dilatant behaviour. The evolution of the fluid pressure during shearing was systematically discussed for the S-tests in Section 3.2.1 (cf. Fig. 6c), and the equivalent curves for all other S-tests are summarized in Fig. 19, again grouped for the three series corresponding to the different stress levels as in Fig. 17. Again it is highlighted that the apparent lower pore pressure generation by Lab C in graph (b) of Fig. 19 can be explained by the lower effective stress level (cf. Figs. 19a, 18). The graphs of Fig. 19 illustrate the nonlinear evolution of the fluid pressure for all the tests during shearing, with the achievement of the maximum value well before the achievement of the maximum deviator stress. In addition, a stabilization of the fluid pressure corresponding
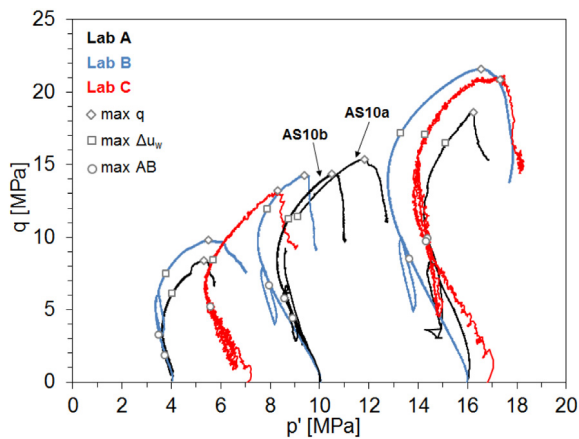
Fig. 18. Comparison of the effective stress paths for all the performed S-tests by the different laboratories.

to the post-peak or ultimate condition was reached in almost all the tests. The similarity of test results between Lab B and Lab C starting from near identical stress level is striking, both in effective stress path (Fig. 18) but also when plotted as pore fluid pressure generation with strain (Fig. 19c). It is emphasized again that Lab B uses the conventional testing method and Lab C the alternative method.

Test results by Lab A yielded similar, but somewhat lower strength (Fig. 17) and fluid pressure generated during loading (Fig. 19) compared to the other two laboratories. This systematic shift appears to be in part related to the fluid pressure loss in the membrane as discussed above. However, Figs. 18 and 19 demonstrate that the repeat test AS10b changes only marginally the pore pressure evolution and the stress path during shear compared to AS10a. Material heterogeneity (cf. Section 2) is unlikely to explain the small difference in test results of Lab A compared to the other labs (cf. Figs. 18 and 19). It may be speculated that some micro-fissures were present in the initial core or induced during sub-coring. But no systematic trend which would support this interpretation is seen in the derived elastic properties (Figs. 15 and 16). System compliance could also be a relevant aspect as discussed under Section 4.1. It appears that the difference in excess pore pressure generated during the tests in comparison with the other two labs increases with increasing effective stress (Fig. 18). Yet another possible explanation could be, that the side drains used by Lab A do not sufficiently dissipate pore fluid pressure generated and hence measured at the fluid pressure sensor. It is true that Lab A did use the lowest strain rate of all laboratories (Table 4), but indeed, if the side drains' contribution to equilibration of pore fluid pressure would be restricted or inhibited entirely (e.g. clogged by indentation into the specimen) a strain rate of approximately 3×10^{-8} s^{-1} would be required. This would be lower by a factor of two to three than the strain rates used (Table 4).

The good agreement of the test results between all laboratories is even more compelling for the P-tests (Fig. 20). Although the tests were performed at different values of initial effective confining stress, the consistency of the experimental results was highlighted by the relationship between the axial stress and axial strain (graph a) in Fig. 20, and by the effective stress paths (graph b) in Fig. 20. Indeed, all the performed P-tests exhibited the same linear evolution of the effective stress path, with an increase of the effective mean stress during loading. Moreover, all the specimens experienced an increase of the fluid pressure almost up to the achievement of the maximum deviator stress, corresponding to the failure of the specimens. These two aspects

marked the most important differences with respect to S-tests and were observed in all the P-tests performed with both the conventional and alternative procedures.

The obtained results demonstrated the robustness of the adopted testing procedures and their capability in providing consistent experimental results. The observed hydro-mechanical response in both S- and P-tests highlighted the capability of both experimental procedures in re-saturating the specimens before the shearing phase. In particular, limiting the volumetric expansion of the specimens below values of 0.1% during the re-saturation in the conventional procedure was demonstrated to effectively prevent possible damage due to the swelling induced by the wetting process.

5. Derivation of material's parameters

Tracking the fluid pressure evolution during the undrained loading phase is fundamental for the identification of the processes governing the response of the specimen up to failure, and to derive robust material parameters. The positive results from diagnostic analyses and agreement of test results as discussed above lend strong support for derivation of robust material parameters based on undrained triaxial testing. In the following, material strength parameters are derived from the test results assuming a simple elasto-plastic material law, fitting Mohr–Coulomb strength parameters for the Opalinus Clay.

Fig. 21 presents the results for the S-tests. Three different regressions are illustrated in the graph: peak strength (referring to the max q points), maximum pore fluid pressure (referring to the max Δu_w points) and maximum AB (referring to the max AB points). The corresponding values of effective intercept cohesion (c') and mobilized shear strength (φ') are reported in the figure. The graph demonstrates the evolution of these parameters during the different phases of deformation. An increase of both the effective cohesion and mobilized shear strength was observed from the starting of the shearing until reaching failure. This indicates a hardening behaviour of the material with apparent mobilization of cohesion and friction up to failure. The max AB envelope highlighted the stress state when the material started to experience a reduction of the rate of increase of the pore fluid pressure, and it can be associated to the onset of the plastic behaviour of the specimens during shearing. The max Δu_w and max q envelopes show similar values of c' and φ', meaning that most of the hardening during the shearing occurred before the achievement of the maximum pore fluid pressure. The good linear trend exhibited by the max q points suggested a good consistency of the results.

Fig. 22 illustrates a final comparison between the S-tests and P-tests for both peak and post-peak strength values. The specimens tested parallel to bedding (P-tests) exhibited slightly higher peak strength than the specimens tested perpendicular to bedding (S-tests). This aspect is mainly related to the effective cohesion, which increased from 2.1 MPa for the S-tests to 3.8 MPa for the P-tests, while the mobilized shear strength did not change significantly (see values reported in Fig. 22a). This feature was not explicitly reported in previous studies on the Opalinus Clay from Mont Terri,[24,39] where one single set of strength parameters was defined for both S and P-tests.

Data related to the post-peak condition were processed taking into account that, as a consequence of the failure, the specimen was divided into two blocks which slid on the inclined shear surface. The normal effective stress σ'_n and the shear stress τ, acting along the shear surface, were calculated evaluating the interaction between the blocks. Moreover, the evolution of the contact surface with the axial displacement was considered. The linear trend of experimental points reported in the τ-σ'_n
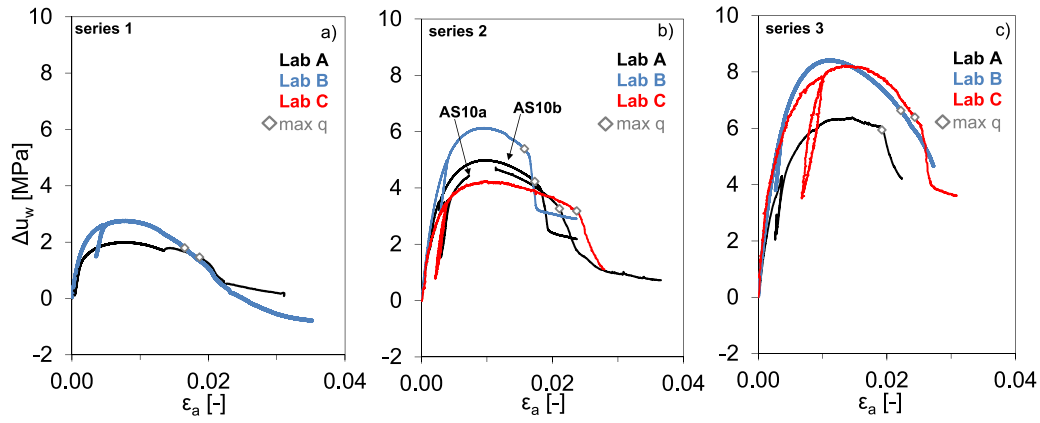
Fig. 19. Evolution of the pore fluid pressure variation with the axial strain during shearing phase of the three series of S-tests performed at different initial effective mean stress p'_{in}. The Lab C tests in the graph (b) and graph (c) were performed at confining effective stress of 7.0 and 16.8 MPa, respectively.
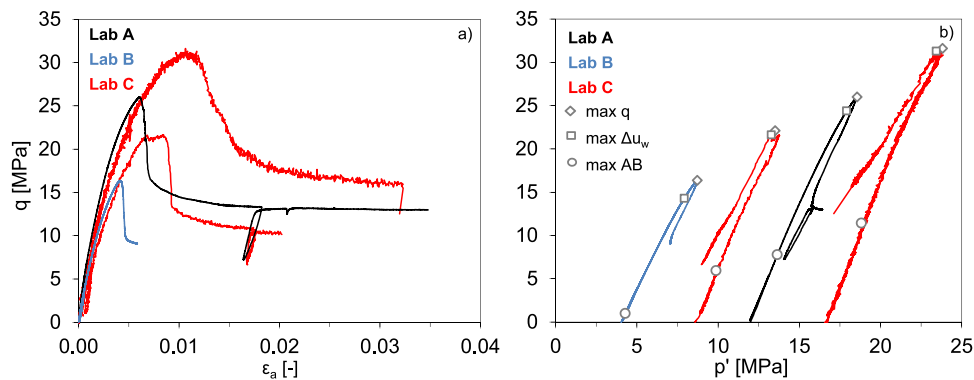
Fig. 20. Experimental results of the P-tests: (a) axial stress–axial strain relationship; (b) effective stress paths.
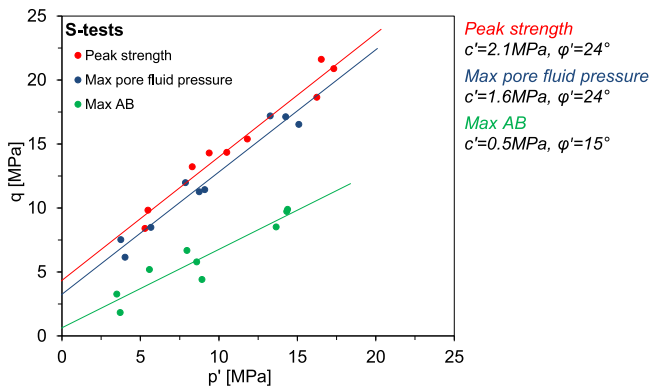
Fig. 21. Strength values obtained with the S-tests along with Mohr–Coulomb envelopes and effective strength parameters.

plane highlights a good overlapping between the two orientations (perpendicular and parallel to bedding); a unique set of Mohr–Coulomb strength parameters was identified and reported in Fig. 22b. This feature was supported by the observed failure plane in the specimens after testing, which was crossing the bedding in both testing configurations, indicating that post-peak strength should indeed be very similar for the two configurations. The reduction of c' to a value close to zero once again suggests a good consistency of the test results. Then, a reduction of both c' and φ' is observed in the post-peak envelope with respect to the peak envelope (Fig. 22b); this feature indicated the weakening of the material's response after failure and the degradation of the

material's strength. The obtained effective strength parameters for the peak and post-peak envelope are indeed similar to those reported in drained tests by Ref. 24.

6. Conclusions

A benchmark experimental study on undrained triaxial testing of the Opalinus Clay was presented. Sample heterogeneity could largely be excluded by detailed inspection of initial cores and confirmation of basic properties and mineralogy of the tested specimens. Sample handling and specimen preparation, and saturation of the specimens were performed very carefully to minimize volume changes and hence potential of specimen damage. The appropriate loading rate was determined, and tests executed with additional margin (lower rate than calculated as appropriate).

On this basis, three different laboratories using two different testing procedures (conventional and alternative) produced very similar test results. The two testing procedures differ for the saturation methodology, where the conventional procedure foresaw fluid injection at constant volume, while the alternative procedure adopted the material equalization to a given value of relative humidity prior to an isotropic undrained compaction. Minor discrepancies in test results appear to be related mainly to technical execution of the testing procedures (membrane initially used by Lab A). The comparison confirmed that both of the adopted testing procedures were sound. The validated test results lend additional confidence in the determination of hydro-mechanical material parameters.

Most importantly, the study demonstrates that robust and reproducible results can be achieved in triaxial testing of shales.
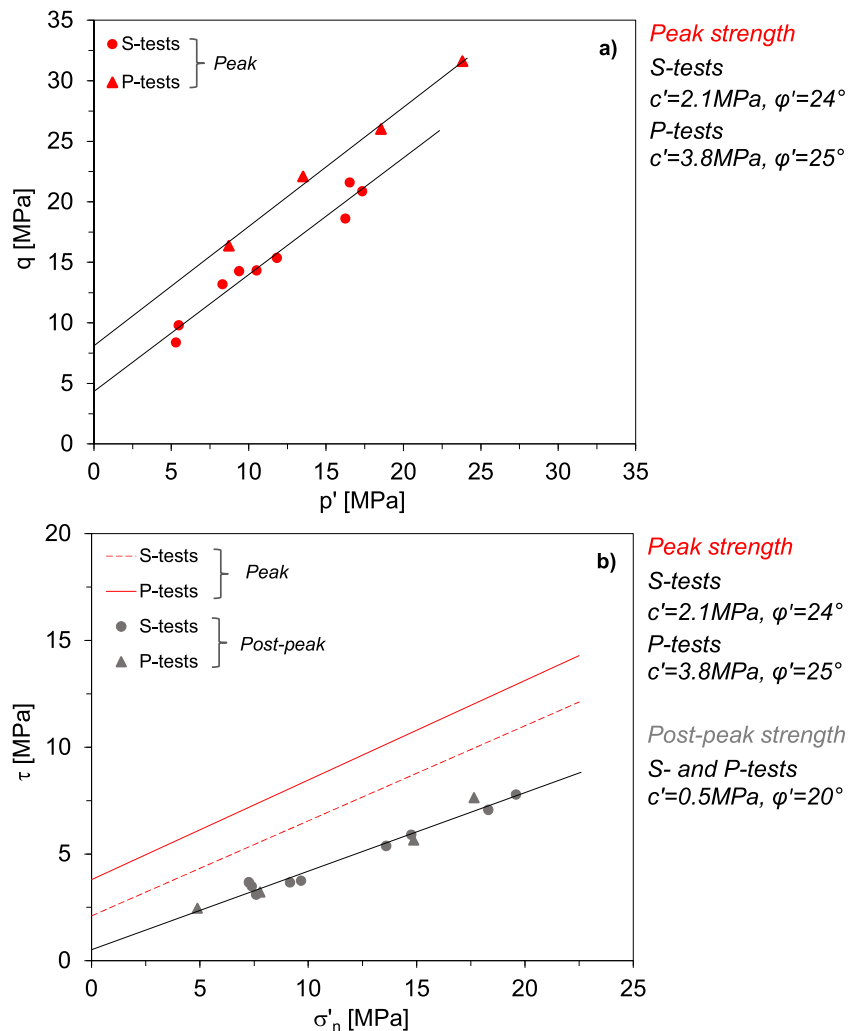
Fig. 22. Comparison of the peak strength values between S-tests and P-tests in the q-p′ plane along with Mohr–Coulomb envelopes. (b) Post-peak strength values of S-tests and P-tests along with Mohr–Coulomb envelopes in the τ-σ'_n plane.

CRediT authorship contribution statement

Alberto Minardi: Formal analysis, Writing - original draft. **Silvio B. Giger:** Funding acquisition, Resources, Project administration, Conceptualization, Writing - review & editing. **Russell T. Ewy:** Methodology, Investigation, Validation, Writing - review & editing. **Rudy Stankovic:** Methodology, Investigation. **Jørn Stenebråten:** Methodology, Validation, Investigation. **Magnus Soldal:** Methodology, Validation, Investigation. **Marco Rosone:** Investigation. **Alessio Ferrari:** Supervision, Writing - review & editing. **Lyesse Laloui:** Supervision.

Declaration of competing interest

The authors declare that they have no known competing financial interests or personal relationships that could have appeared to influence the work reported in this paper.

Acknowledgements

References

1. Ulusay R, Hudson JA eds, *The Complete ISRM Suggested Methods for Rock Characterization, Testing and Monitoring: 1974-2006 [Blue Book].* Ankara: ISRM Turkish National Group; 2007.
2. Ewy RT. Shale/claystone response to air and liquid exposure, and implications for handling, sampling and testing. *Int J Rock Mech Min Sci.* 2015;80:388–401.
3. Espitia JM, Caicedo B, Vallejo L. Effect of suction and stress on Poisson's ratio of argillaceous rocks. *Géotech Lett.* 2017;7:53–59.
4. Ewy RT. Mechanical anisotropy of gas shales and claystones. In: *Fourth EAGE Shale Workshop.* 2014.
5. Menaceur H, Delage P, Tang AM, Conil N. The thermo-mechanical behaviour of the Callovo-Oxfordian claystone. *Int J Rock Mech Min Sci.* 2015;78:290–303.
6. Pham QT, Valès F, Malinsky L, Nguyen Minh D, Gharbi H. Effects of desaturation–resaturation on mudstone. *Phys Chem Earth A/B/C.* 2007;32:646–655.
7. Valès F, Nguyen Minh D, Gharbi H, Rejeb A. Experimental study of the influence of the degree of saturation on physical and mechanical properties in Tournemire shale (France). *Appl Clay Sci.* 2004;26:197–207.
8. Zhang F, Xie SY, Hu DW, Shao JF, Gatmiri B. Effect of water content and structural anisotropy on mechanical property of claystone. *Appl Clay Sci.* 2012;69:79–86.

9. Wild KM, Wymann LP, Zimmer S, Thoeny R, Amann F. Water retention characteristics and state-dependent mechanical and petro-physical properties of a clay shale. *Rock Mech Rock Eng*. 2014:1–13.

10. Chiu HK, Johnston IW, Donald IB. Appropriate techniques for triaxial testing of saturated soft rock. *Int J Rock Mech Min Sci Geomech Abstr*. 1983;20-3:107–120.

11. Ferrari A, Minardi A, Ewy R, Laloui L. Gas shales testing in controlled partially saturated conditions. *Int J Rock Mech Min Sci*. 2018;107:110–119.

12. Minaeian V, Dewhurst DN, Rasouli V. Deformational behaviour of a clay-rich shale with variable water saturation under true triaxial stress conditions. *Geomech Energy Environ*. 2017;11:1–13.

13. Minardi A, Ferrari A, Ewy R, Laloui L. Nonlinear elastic response of partially saturated gas shales in uniaxial compression. *Rock Mech Rock Eng*. 2018;51:1967–1978.

14. Ferrari A, Favero V, Marschall P, Laloui L. Experimental analysis of the water retention behaviour of shales. *Int J Rock Mech Min Sci*. 2014;72:61–70.

15. Minardi A, Ferrari A, Ewy R, Laloui L. The impact of the volumetric swelling behavior on the water uptake of gas shale. *J Nat Gas Sci Eng*. 2018b;49:132–144.

16. Minardi A, Crisci E, Ferrari A, Laloui L. Anisotropic volumetric behaviour of opalinus clay shale upon suction variation. *Géotech Lett*. 2016;6:144–148.

17. Pineda JA, Alonso EE, Romero E. Environmental degradation of claystones. *Géotechnique*. 2014;64(1):64–82.

18. Pineda JA, Romero E, De Gracia M, Sheng D. Shear strength degradation in claystones due to environmental effects. *Géotechnique*. 2014;64(6):493–501.

19. Ewy RT. Shale swelling/shrinkage and water content change due to imposed suction and due to direct brine contact. *Acta Geotech*. 2014:1–18.

20. Ewy RT. Practical approaches for addressing shale testing challenges associated with permeability, capillarity and brine interactions. *Geomech Energy Environ*. 2018;14:3–15.

21. Belmokhtar M, Delage P, Ghabezloo S, Conil N. Drained triaxial tests in low-permeability shales: Application to the callovo-oxfordian claystone. *Rock Mech Rock Eng*. 2018;51:1979–1993.

22. Giger SB, Ewy RT, Favero V, Stankovic R, Keller LM. Consolidated-undrained triaxial testing of opalinus clay: Results and method validation. *Geomech Energy Environ*. 2018;14:16–28.

23. Wild KM, Barla M, Turinetti G, Amann F. A multi-stage triaxial testing procedure for low permeable geomaterials applied to opalinus clay. *J Rock Mech Geotech Eng*. 2017;9:519–530.

24. Favero V, Ferrari A, Laloui L. Anisotropic behaviour of opalinus clay through consolidated and drained triaxial testing in saturated conditions. *Rock Mech Rock Eng*. 2018;51:1305–1319.

25. Steiger RP, Leung PK. Consolidated undrained triaxial test procedure for shales. In: *32nd U.S. Rock Mech. Symp.*. 1991:637–646.

26. Ewy RT, Stankovich RJ, Bovberg CA. Mechanical behavior of some clays and shales from 200 m to 3800 m depth. In: *39th US Rock Mechanics Symposium/12th Panamerican Conference Soil Mech & Geotech Eng*. Cambridge, USA: MIT; 2003:22–26.

27. Fredlund DG. Density and compressibility characteristics of air–water mixtures. *Can Geotech J*. 1976;13(4):386–396.

28. Bossart P, Thury M. *Mont Terri Rock Laboratory – Project, Programme 1996 to 2007 and Results*. Reports of the Swiss Geological Survey No. 3, Wabern: Swiss Geological Survey; 2008.

29. Keller LM, Giger SB. Petrophysical properties of Opalinus Clay drill cores determined from med-XCT images. *Geotech. Geol. Eng.*. 2019. http://dx.doi.org/10.1007/s10706-019-00815-2.

30. Favero V, Ferrari A, Laloui L. On the hydro-mechanical behaviour of remoulded and natural Opalinus Clay shale. *Eng Geol*. 2016;208:128–135.

31. Ferrari A, Favero V, Laloui L. One-dimensional compression and consolidation of shales. *Int J Rock Mech Min Sci*. 2016;88:286–300.

32. Skempton AW. The pore-pressure coefficients A and B. *Géotechnique*. 1954;4:143–147.

33. Wersin P, Mazurek M, Waber HN, UrsK Mäder, Gimmi T, Rufer D, de Haller A. Rock and porewater characterisation on drillcores from the Schlattingen borehole. In: *Nagra Arbeitsbericht NAB 12-054*. 2013.

34. Berre T. Triaxial testing of soft rocks. *Geotech Test J*. 2011;34(1):61–75.

35. Nes OM, Sonstebo EF, Fjaer E, Holt RM. *Use of Small Shale Samples in Borehole Stability Analysis*. American Rock Mechanics Association; 2004 ARMA-04-564.

36. Head KH. *Manual of Soil Laboratory Testing*. In: Effective stress tests, 2nd ed. vol. 3, Chichester: Manual of soil laboratory testing. Wiley; 1998.

37. Renner J, Evans B, Hirth G. On the rheologically critical melt fraction. *Earth Planet Sci Lett*. 2000;181:585–594.

38. Fjær E, Stroisz AM, Holt RM. Elastic dispersion derived from a combination of static and dynamic measurements. *Rock Mech Rock Eng*. 2013;46:611–618.

39. Wild KM, Amann F. Experimental study of the hydro-mechanical response of Opalinus Clay–Part 1: Pore pressure response and effective geomechanical properties under consideration of confinement and anisotropy. *Eng Geol*. 2018;237:32–41.